On The Cellular Structure Of Carbon Detonations

F. X. Timmes[1,2], M. Zingale[1,2], K. Olson[1,3], B. Fryxell[1,3], P. Ricker[1,2], A. C. Calder[1,2], L. J. Dursi[1,2], H. Tufo[1], P. MacNeice[4], J. W. Truran[1,2,3], R. Rosner[1,2,3]

Received _____; accepted _____

[1]Center for Astrophysical Thermonuclear Flashes, The University of Chicago, Chicago, IL 60637

[2]Dept. of Astronomy & Astrophysics, The University of Chicago, Chicago, IL 60637

[3]Enrico Fermi Institute, The University of Chicago, Chicago, IL 60637

[4]NASA Goddard Space Flight Center, Greenbelt, MD 20771

ABSTRACT

We present the results of a numerical study on two-dimensional carbon detonations. For an upstream density of 10^7 g cm^{-3} the length-to-width ratio of the detonation cells is about 1.6 and is not strongly dependent on the spatial resolution of the simulation. However, the curvature of the weak incident shocks, strength of the triple points and transverse waves, and sizes of the under-reacted and over-reacted regions all depend strongly on the spatial resolution of the calculation. These resolution studies help define the minimum resolution required by multidimensional Type Ia supernovae models where the cellular structure of a detonation front is a key feature of the model.

Subject headings: hydrodynamics– instabilities – nuclear reactions – shock waves – supernovae: general

1. Introduction

The simplest one-dimensional theory of detonations was formulated about a century ago by Chapman (1899) and Jouguet (1905). The laminar detonation front is assumed to be a jump discontinuity, a shock in which the reactants go to completion instantaneously. The Chapman-Jouguet (CJ) solution specifies the unique, minimum speed of the detonation front, along with the thermodynamic states just behind the incident shock and where the ashes reach their equilibrium values. Despite the wealth of information returned by the CJ solution, it does not give the width of the shock-to-equilibrium region, spatial variations of the thermodynamic or hydrodynamic variables within the burning region, or if the solution is the self-sustaining detonation solution. These deficiencies were removed by Zeldovich (see Ostriker 1992), von Neumann (1942) and Döring (1943), who formulated

three ordinary differential equations to be solved. Their treatment is called the ZND model of a detonation. In the ZND model, the flow is assumed to one-dimensional with the shock still treated as a discontinuity, but now one in which the reactants are triggered by the passage of the shock and proceed at finite rates thereafter. The ZND solutions give the width of the detonation, and the spatial variation of the thermodynamic and hydrodynamic variables for self-sustaining or over-driven detonations. In addition, the global integrals of the ZND equations reduce to the algebraic CJ relations.

Detonation experiments in the middle of the last century clearly showed that a real detonation wave has a complex, multidimensional, time-dependent structure (Fickett & Davis 1979). The one-dimensional, planar detonation front becomes unstable to longitudinal perturbations in the density and is replaced by incident shocks, transverse waves, and triple-points that interact and continuously change. Despite the fact that a real detonation is far from the steady, one-dimensional motion given by the CJ and ZND models, the average speed of the multidimensional detonation front travels at nearly ($\sim$ 1-2% less than) the CJ value.

A schematic illustrating the essential features of a real detonation wave is shown in Figure 1. The detonation front is depicted by the orange curves at three different times $t1 > t2 > t3$. Instead of a uniform planar surface, a detonation front is composed of alternate sections of weak incident shocks and triple points. The weak incident shocks have significant curvature and are not powerful enough to sustain the detonation; it is the triple points that drive the propagation. The triple points, shown as blue ellipses in Figure 1, form a a grid of regularly spaced hot spots that move across the front. and act as a set of miniture spherical detonations. Emanating from the triple points are shock waves, called transverse waves, that have a velocity component that is large and nearly perpendicular to the detonation front. The transverse waves are depicted as the green curves in Figure 1, and are a key

feature of real detonations. In time, the transverse waves move back and forth across the detonation front. They are not steady waves, but are continually decaying, and stay alive only by periodic rejuvenation through collisions with other transverse waves moving in the opposite direction (Fickett & Davis 1979). Each collision creates a new high-pressure region, a new triple point. The receding transverse waves move into the now weakened old triple points and become the incident shocks for the new triple points. In other words, at each transverse wave collision the triple point and incident shock are, in effect, interchanged. A detonation propagates forward primarily by moving laterally. Superimposed on the key features of a detonation in Figure 1 are the trajectories of the triple points, shown as the black curves. It is these high pressure point trajectories that give rise to the characteristic cellular (or fish-scale) pattern recorded by terrestrial experiments.

While there have been many experiments and calculations for detonations in terrestrial materials, the role of the cellular structure of detonations in astrophysics has not been fully explored, particularly with regard to models for X-ray bursts and Type Ia supernovae. There are only two such studies to date that apply in astrophysical environments. Boisseau et al. (1996) reported the first results of two-dimensional detonations in degenerate carbon-oxygen matter typical of white dwarfs. They showed that the longitudinal instabilities induce transverse waves that interact and create pockets of incompletely burned material. These pockets, or cells, increase the effective size of the burning region, slightly reduce the detonation velocity, and produces a different composition distribution in the detonated material relative to those predicted by one-dimensional calculations. Gamezo et al. (1999) presented two-dimensional detonations in degenerate carbon-oxygen material over a range of upstream densities. They found a multicellular structure, with cell size hierarchy corresponding to carbon burning (smallest cells), oxygen burning, and silicon burning (largest cells). For densities below 10^7 g cm^{-3}, the size of their silicon cells are comparable to or larger than the size of a white dwarf. They suggested that the

concentration fluctuations that exist within the cell hierarchy may affect the spectra of Type Ia supernovae predicted by delayed-detonation models.

The primary purpose of this paper is to assess the structure of the weak incident shocks, triple points, transverse waves, and cell sizes on the spatial resolution employed in the calculation. By varying the spatial resolution from 10^{-1} cm to 1.25×10^{-2} cm (a factor of 8 in one-dimension or a factor of 64 in area), we demonstrate convergence of the flow features.

In §2 the computational methods and input physics used to determine cellular detonation structure are discussed. In §3 the physical properties of the cellular carbon detonations, their sensitivity to the computational methods, and comparison to previous calculations are presented. A summary of the results is given in §4.

2. Methods, Input Physics, Initial Conditions, and Boundary Conditions

The FLASH code (Fryxell et al. 2000) is used to obtain the two-dimensional solutions to the reactive flow equations. FLASH is a modular, adaptive mesh, parallel simulation code capable of handling general compressible flow problems in astrophysical environments. It uses the PARAMESH library (MacNeice et al. 2000) to manage a block-structured adaptive grid, placing resolution elements only where they are needed in order to track narrow flow features, such as shocks. The compressible Euler equations are solved using an explicit, directionally split version of the piecewise-parabolic method (Colella & Woodward 1984), which allows for general equations of state using the method of Colella & Glaz (1985). An equation of state appropriate to stellar interiors is implemented using a thermodynamically consistent table lookup scheme (Timmes & Swesty 1999). Source terms for thermonuclear reactions are solved using a semi-implicit time integrator coupled to a sparse matrix solver

(Timmes 1999). FLASH is implemented in Fortran 90 and uses the Message-Passing Interface library to achieve scalability on a variety of different message-passing parallel computers. Further details concerning the algorithms used in the code, the code's structure, and results of verification tests may be found in Fryxell et al. (2000).

A 13 isotope α-chain plus heavy-ion reaction network was used in the calculations. A definition of what we mean by an α-chain reaction network is prudent. A strict α-chain reaction network is only composed of (α,γ) and (γ,α) links among the 13 isotopes ^{4}He, ^{12}C, ^{16}O, ^{20}Ne, ^{24}Mg, ^{28}Si, ^{32}S, ^{36}Ar, ^{40}Ca, ^{44}Ti, ^{48}Cr, ^{52}Fe, and ^{56}Ni. It is essential, however, to include (α,p)(p,γ) and (γ,p)(p,α) links in order to obtain reasonably accurate energy generation rates and abundance levels when the temperature exceeds $\sim 2.5\times10^{9}$ K. At these elevated temperatures the flows through the (α,p)(p,γ) sequences are faster than the flows through the (α,γ) channels. An (α,p)(p,γ) sequence is, effectively, an (α,γ) reaction through an intermediate isotope. In our α-chain reaction network, we include 8 (α,p)(p,γ) sequences plus the corresponding inverse sequences through the intermediate isotopes ^{27}Al, ^{31}P, ^{35}Cl, ^{39}K, ^{43}Sc, ^{47}V, ^{51}Mn, and ^{55}Co by assuming steady state proton flows. This strategy permits inclusion of (α,p)(p,γ) sequences without explicitly evolving the proton or intermediate isotope abundances. Thus, the α-chain reaction network in FLASH includes not just (α,γ) and (γ,α) links, but also links through the (α,p)(p,γ) and (γ,p)(p,α) sequences. How well this small reaction network mimics the nuclear energy generation rate given by a large 489 isotope reaction network is analyzed in (Timmes, Hoffman, & Woosley 2000).

The two-dimensional calculations were performed in planar geometry, a choice motivated by a desire to facilitate comparisons to the Boisseau et al. (1996) and Gamezo et al. (1999) simulations, which were also carried out in planar geometry. The radial dimension of the white dwarf is also large compared to the thickness of a detonation wave's

main energy producing region at the density of interest in this work, so curvature effects should be small.

The initial conditions consisted of a constant density of 10^7 g cm^{-3}, temperature of 2×10^8 K, composition of pure carbon X(^{12}C)=1, and material velocity of v_x=v_y= 0 cm s^{-1}. The choice for the upstream temperature is not critical due to the weak temperature dependence of the pressure and specific internal energy of the degenerate material. The choice of the upstream density, however, is crucial since it strongly effects the width of the detonation front. Our choice of the density is motivated by the fact that the deflagration-to-detonation transition in delayed-detonation models of Type Ia supernova are typically set occur roughly at 10^7 g cm^{-3}. For it is at this density that the full width of a steady state, self-sustained, ZND detonation is about the same size as the radius of the underlying white dwarf (Khokhlov 1989).

Near the x=0 boundary the initial conditions were perturbed to the values given by the appropriate Chapman-Jouguet solution: a density of 4.236×10^7 g cm^{-3}, temperature of 4.423×10^9 K, and material velocity of $v_x = 2.876\times10^8$ cm s^{-1}. Figure 2 shows the pressure field of the initial conditions for a domain size of 256.0 cm by 25.0 cm. The values and shape of the perturbation are not critical, provided enough carbon is initially ignited to sustain the detonation. Choosing different values or different extents of the perturbation simply change how long it takes for the initial conditions to achieve a near ZND state. Figure 2 also shows the block structure of the mesh. Each block contains 8 grid points in the x-direction, and 8 grid points in the y-direction. The entire mesh is rather coarse at t=0, refining only the shocked interface.

The initial conditions and perturbation given above ignite the nuclear fuel, accelerate the material, and produce an over-driven detonation that propagates along the x-axis. The initially over-driven detonation is damped to a near ZND state on short time-scale.

After some time, which depends on the spatial resolution and boundary conditions, longitudinal instabilities in the density cause the planar detonation to evolve into a complex, time-dependent structure. Figure 3 shows the pressure field of the detonation after 1.26×10^{-7} s. The interacting transverse wave structures are particularly vivid, and extend about 25 cm behind the shock front. Variations in the thermodynamic variables and composition damp out with the distance behind the shock. Full equilibration, so that the reactive flows essentially match the one-dimensional ZND solution, take a larger distance – about 50 cm behind the shock front in Figure 3. The corresponding block structure of the mesh is also shown in Figure 3. The mesh is not refined ahead of the detonation front, maximally refined throughout the reactive regions, and derefined behind the detonation front as the fluid flows becomes smooth.

Periodic boundary conditions were used at the walls parallel to the y-axis while reflecting boundary conditions were used for the walls parallel to the x-axis. A few calculations were conducted with relecting boundary conditions at all the walls. While reflecting boundary conditions allow the initial conditions to relax more quickly and form cellular structures sooner, they have the undesirable effect of having shocks bounce off the walls. This can give rise to spurious structures that would not be present if a larger domain were modeled. Periodic boundary conditions take a relatively longer time to relax the initial conditions and form their cellular structures later, in agreement with Boisseau et al. (1996). While not subject to shocks rebounding from hard walls, periodic boundary conditions can give a false sense of symmetry. All of the boundary conditions, however, produce cell structures of the same size, as found by Boisseau et al. (1996).

3. Results and Discussion

The energy released by burning near the shock front plays a crucial role in the setting the time and length scales of a detonation. For the pure carbon composition we are considering, the ^{12}C+^{12}C heavy-ion reaction is the first reaction to occur, and provides most of the initial energy release. For the thermodynamic conditions just behind the shock we find ρ=4.236×10^{7} g cm^{-3} and T=4.423×10^{9} K. The thermonuclear energy generation rate at these conditions is $\epsilon_{\rm nuc}$=3.167×10^{26} erg g^{-1} s^{-1} and scales locally as $\epsilon_{\rm nuc} \sim {\rm X}(^{12}{\rm C})^2\ \rho^2\ {\rm T}^{16}$. The burning time-scale associated with this energy generation rate is $\tau_{\rm burn} \sim E/\epsilon_{\rm nuc} \sim 2\times10^{-9}$ s, where E is the specific internal energy. The burning length-scale is $L_{\rm burn} \sim v_{\rm det}\ \tau_{\rm burn} \sim 2$ cm, where $v_{\rm det}$ is the speed of the detonation front.

Spatial resolutions of 1×10^{-1} cm, 5×10^{-2} cm, 2.5×10^{-2} cm, and 1.25×10^{-2} were used to examine the dependence of the flow features on resolution. These spatial resolutions span a factor of 64 in area. For a 2 cm burning length-scale, these resolutions correspond to 20, 40, 80, and 160 grid points per burning length-scale. The finest resolutions that we consider would be prohibitively expensive on a uniform mesh. The adaptive mesh algorithms in FLASH place the finest meshes only where they are needed (see Figure 3), thus permitting an analysis of the results at the highest resolutions.

The weak incident shocks, transverse waves, and triple points are prominent features of the pressure fields shown in Figures 4 and 5. Each plot is at at 1.85×10^{-7} s, but Figure 4 has a spatial resolution of 10^{-1} cm , while Figure 5 has a resolution of 1.25×10^{-2} cm. The triple points appear as dark red near the head of the detonation, and are labeled by the dark red arrows in Figure 5. Between the triple points are the weak incident shocks, that are labeled by the black arrows. The transverse waves are quite pronounced in these figures as the triangular structures that are nearly perpendicular to the detonation front. Some of the transverse waves are indicated by the black arrows in Figure 5. There are

appreciable variations in the pressure within the detonation structure, and a sharp visual contrast between the two spatial resolutions.

In Figures 4 and 5, and all of the remaining plots, it is useful to note that the positions of the flow features do not converge as the resolution is increased. This is because the time at which the detonation front develops a steady-state cellular structure is different. At low spatial resolutions it takes a longer time for the long wavelength modes of the instabilities to grow, deform the detonation front, and saturate. At high resolutions the shorter wavelength modes grow quicker, deform the planar surface sooner, and achieve steady-state faster Thus, we seek convergence in the magnitude of the flow features, not in their positions.

The corresponding temperature fields at the two resolutions is shown in Figures 6 and 7. Some of the triple points, weak incident shocks, and transverse waves are labelled. The weak incident shock waves do not increase the temperature enough to sustain the detonation front. Only at the triple points, where the temperatures and pressures are much larger, is enough energy generated by burning to sustain the detonation front. The lower resolution model, Figure 6, shows almost no vorticity, while the higher resolution case, Figure 7, shows significant vorticity. Collisions between the transverse waves generate the vorticity. These pockets of cooler material and hotter material generate pockets have lower and high energy generation rates, respectively. In the high temperature regions the material will be turned to ash faster than in the cooler pockets. Figures 6 and 7 suggest that the curvature of the weak incident shocks, strength of the triple points and transverse waves, and sizes of the high temperature and low-temperature regions all depend strongly on the spatial resolution of the calculation.

The corresponding carbon (the fuel) mass fraction fields at the two resolutions is shown in Figures 8 and 9, while the silicon (the ash) mass fraction fields are shown in Figures 10 and 11. There are under-reacted regions containing more fuel than ash, and over-reacted

regions containing more ash than fuel. The under-reacted regions are from material behind the weak incident shocks that are cut off by the collision of two transverse waves, while the over-reacted regions are from the triple points. These under-reacted and over-reacted regions move downstream and gradually disappear (see Figure 3) due to mixing by the vortices, continuation of the nuclear reactions to their final equilibrium ash state (nuclear statistical equilibrium), and numerical diffusion. Similar under- and over-reacted pockets are observed in terrestrial experiments (e.g., Strehlow 1968) and simulations of terrestrial detonations (e.g., Oran et al. 1992).

Figures 12 – 15 show the maximum pressure reached at each point in space for all time for each of the spatial resolutions we examined. The temporal resolution in each of these "smoke-foil" plots is 5×10^{-11} s, which is still coarse enough to cause the striation visible in the figures with the higher spatial resolutions. In effect, these plots are movies where every frame is overlayed with each other and the maximum pressure reached by any point recorded. Similar cell structures are produced in terrestrial experiments by passing chemical detonations over a coated surface (e.g. soot over metal).

The cellular patterns in Figures 12 – 15 result from the trajectories of the high pressures generated at the triple points (see the schematic of Figure 1). The size of the cell is correlated with the nuclear burning time scale (or length scale); the longer the burning time-scale the bigger the cells. The length of each cell along the x-axis is about 6.0 cm, while the width along the y-axis is about 3.8 cm. The figures show the length-to-width ratio of 1.6 is not strongly dependent on the spatial resolution. At higher resolutions some irregularity in the pattern formed by the high pressure cells emerges as the flow features become more defined.

3.1. Comparison with Other's Results

Gamezo et al. (1999) presented two-dimensional simulations of detonations in material that was half carbon, X(^{12}C) = 0.5, and half oxygen, X(^{16}O) = 0.5, and spanned a density range between 10^6 and 3×10^7 g cm^{-3}. Gamezo et al. (1999) used a mesh size of 0.1 cm at a density of 10^7 g cm^{-3}, corresponding to about 10 grid points per burning length scale (see §2), and found a detonation cell size of 7.0 cm. They claimed the dimensions of their cell sizes were resolution dependent, being perhaps 2-3 times larger than the cell sizes determined from higher numerical resolutions.

Our simulations are also two-dimensional and conducted in planar geometry, but are for detonations in pure carbon, X(^{12}C) = 1.0, at a density 10^7 g cm^{-3}. For a mesh size of 0.1 cm, which is the coarsest resolution we consider, we find a cell length of about 6.0 cm and a cell width of abount 3.8 cm.

It is known (Fickett & Davis 1979) that the size of the detonation cells in terrestrial chemical systems follows the one-dimensional burning length scale. If the same scaling applies for astrophysical nuclear systems, then one might expect the cell sizes to vary as X(^{12}C)^2. If this is the case, then there might be a discrepancy between the cell sizes calculated by Gamezo et al. (1999) for carbon-oxygen material and the cell sizes we calculate for pure carbon material. Either their cell sizes might be too small by a factor 4 or our cell lengths might be too large by a factor of 4. It is also possible that there is no discrepency, since for either composition carbon burning provides the initial energy source that sustains the detonation. That Gamezo et al. (1999) calculates a cell length of 7.0 cm for a half-carbon half-oxygen composition while we find 6.0 cm for a pure carbon composition may support this conjecture. In addition, the ashes of carbon burning (primarily ^{20}Ne and α-particles) will also burn. Thus while the cell sizes may scale with the one-dimensional burning length scale, the burning length scale may not scale as simply as

$X(^{12}C)^2$.

Perhaps related to this possible discrepency is that while we find the cell lengths are larger than the cell widths, the results of Gamezo et al. (1999) seem to indicate that the cell lengths are equal to the cell widths. In addition, we find that the dimensions of the cell are not strongly dependent on the spatial resolution, as comparison of Figures 12 – 15 indicate. In fact, our results would suggest that convergence of the cell sizes has already been reached at a mesh size of 0.1 cm. While the cell sizes are fairly constant as a function of spatial resolution, Figures 12 – 15 suggest some irregularity appears as the flow features become more resolved.

4. Summary

We have found that the cell sizes of a two-dimensional detonation propagating through pure carbon at 10^7 g cm^{-3} are robust with respect to the spatial resolution of the simulation. The cell length of 6.0 cm is larger than the cell width of 3.8 cm. The cell length to width ratio is thus about 1.6 for this density and composition, which is also about the ratio of the average material velocity in the direction of the propagation to the average material velocity in the transverse direction.

The average curvature of the weak incident shocks, average strength of the triple points and transverse waves, and average sizes of the under-reacted and over-reacted regions are all strongly dependent on the spatial resolution of the simulation.

Since the cell sizes are much smaller than the pressure scale height in a white dwarf at this density and composition, we expect the under- and over-reacted pockets at 10^7 g cm^{-3} to have a negligible effect on the spectra of a Type Ia supernova, or on their resulting nucleosynthesis. As recognized by Boisseau et al. (1996) and Gamezo et al. (1999), the

cases which might have the largest impact on the spectra and nucleosynthesis are those in which the cell size is comparable to the size of the underlying white dwarf, or perhaps even the smaller size of the density scale height.

Our results help to define the minimum resolution required by multidimensional Type Ia supernovae models where a cellular detonation is a key feature of the model. In the near future we will show the composition dependence of the cell sizes in carbon-oxygen detonations, and the flow structures of three-dimensional carbon detonations.

This work is supported by the Department of Energy under Grant No. B341495 to the Center for Astrophysical Thermonuclear Flashes at the University of Chicago.

REFERENCES

Boisseau, J. R., Wheeler, J. C., Oran, E. S., & Khokhlov, A. M. 1996, ApJ, 471, L99

Chapman, D. L. 1899, Philos. Mag., 47, 90

Colella, P. & Glaz, H. M. 1985 JCP, 59, 264

Colella, P. Woodward, P. 1984 JCP, 54, 174

Döring, W. 1943, Ann. Phys., 43, 421

Fickett, W. & Davis, W. C. 1979, Detonation, (Berkeley: Univ. California Press)

Fryxell, B. A., et al. 2000, ApJS, in press

Gamezo, V. N., Wheeler, J. C., Khokhlov, A. M., & Oran, E. S. 1999, ApJ, 512, 827

Jouguet, E. 1905, J. de Mathematiques Pures at Appliquees, 1, 347

Khokhlov, A. M. 1989, MNRAS, 239, 785

MacNeice, P., Olson, K. M., Mobarry, C., de Fainchtein, R., & Packer, C. 2000, Computer Physics Communications, in press

Oran, E. S., Young, T. R., Boris, J. P., Picone, J. M., & Edwards, D. H. 1992, in Proc. 19th Int. Symp. on Combustion, 573

Ostriker, J. P. 1992, Selected works of Yakov Borisovich Zeldovich, (Princeton Univ. Press, Princeton N.J.)

Strehlow, R. A. 1968, Combust. Flame, 12 81

Timmes, F. X. 1999, ApJS, 124 241

Timmes, F. X., Hoffman, R. D., & Woosley, S. E. 2000, ApJS, in press

Timmes, F. X., & Swesty, F. D. 2000, ApJS, in press

Von Neumann, J. 1942, OSRD Rep. No. 549

This manuscript was prepared with the AAS LaTeX macros v5.0.

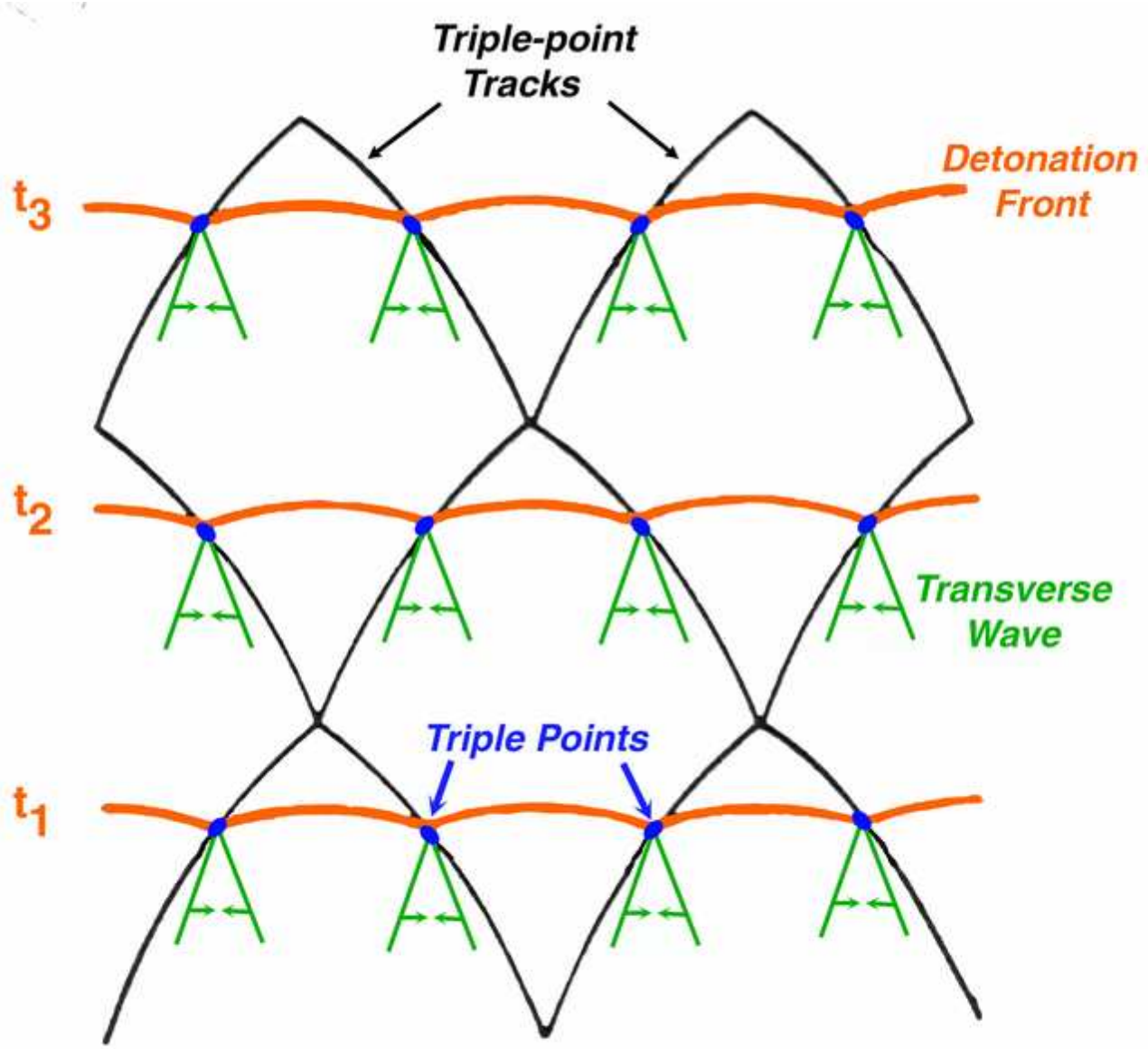

Fig. 1.— Schematic showing the main features of a detonation. Orange curves depict the detonation front at three times, $t1 > t2 > t3$. Blue ellipses mark the triple points, green lines illustrate the transverse waves, and the trajectories of the triple points are marked in black.

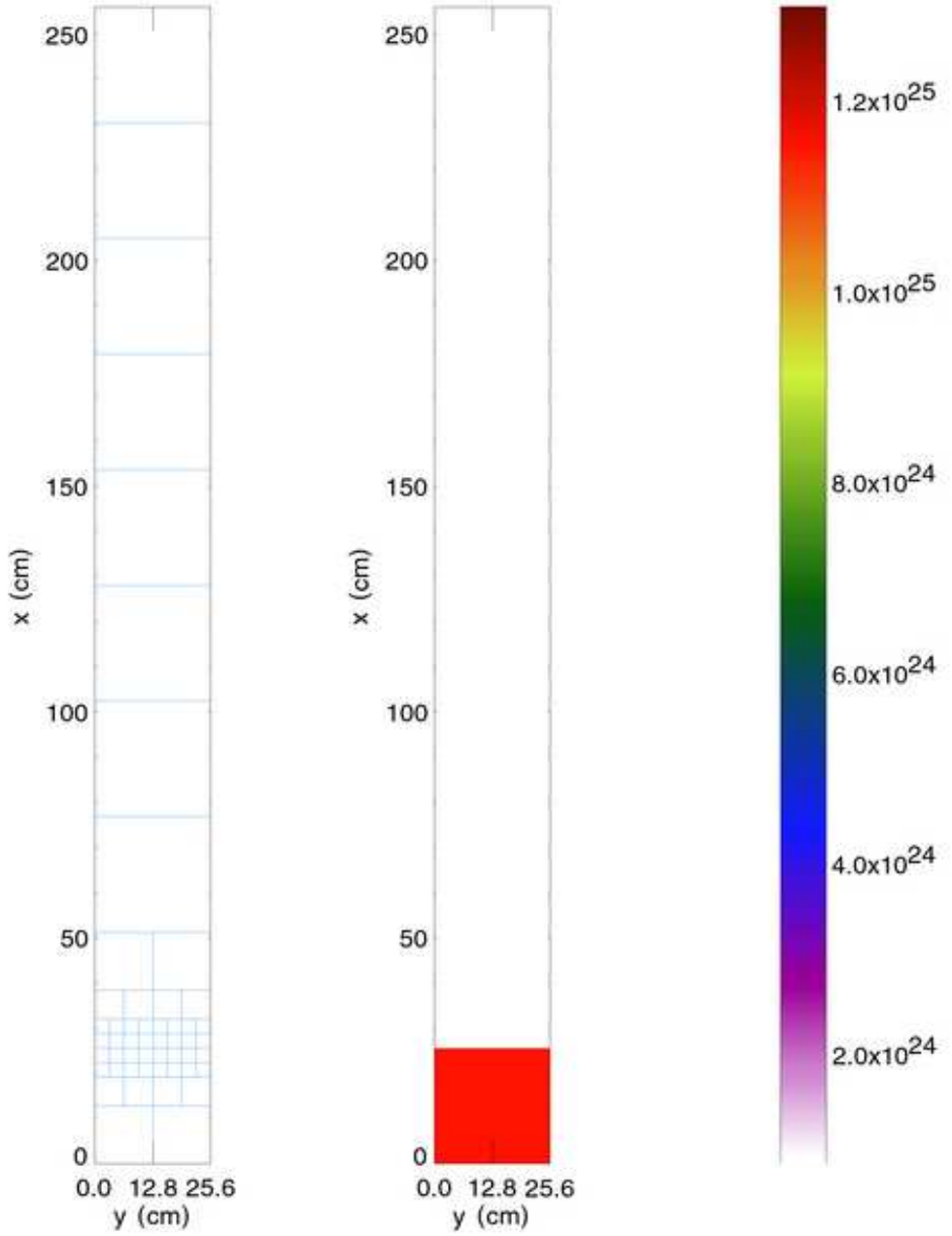

Fig. 2.— Pressure field for the initial conditions. The legend to the right of the plot gives the magnitude of the pressure in erg cm^{-3} on a linear scale. Superimposed on the upstream density of 10^7 g cm^{-3}, temperature of 2×10^8 K, composition of pure carbon X(^{12}C)=1, and material velocity of $v_x = v_y = 0$ cm s^{-1} is the ZND solution just behind the shock (ρ=4.236×10^7 g cm^{-3}, T=4.423×10^9 K, and v_x=2.876×10^8 cm s^{-1}). The carbon ignites and drives a detonation wave that propagates along the x-axis. Also shown are the computational blocks. Each block contains 8 grid points in the x-direction and 8 grid points in the y-direction.

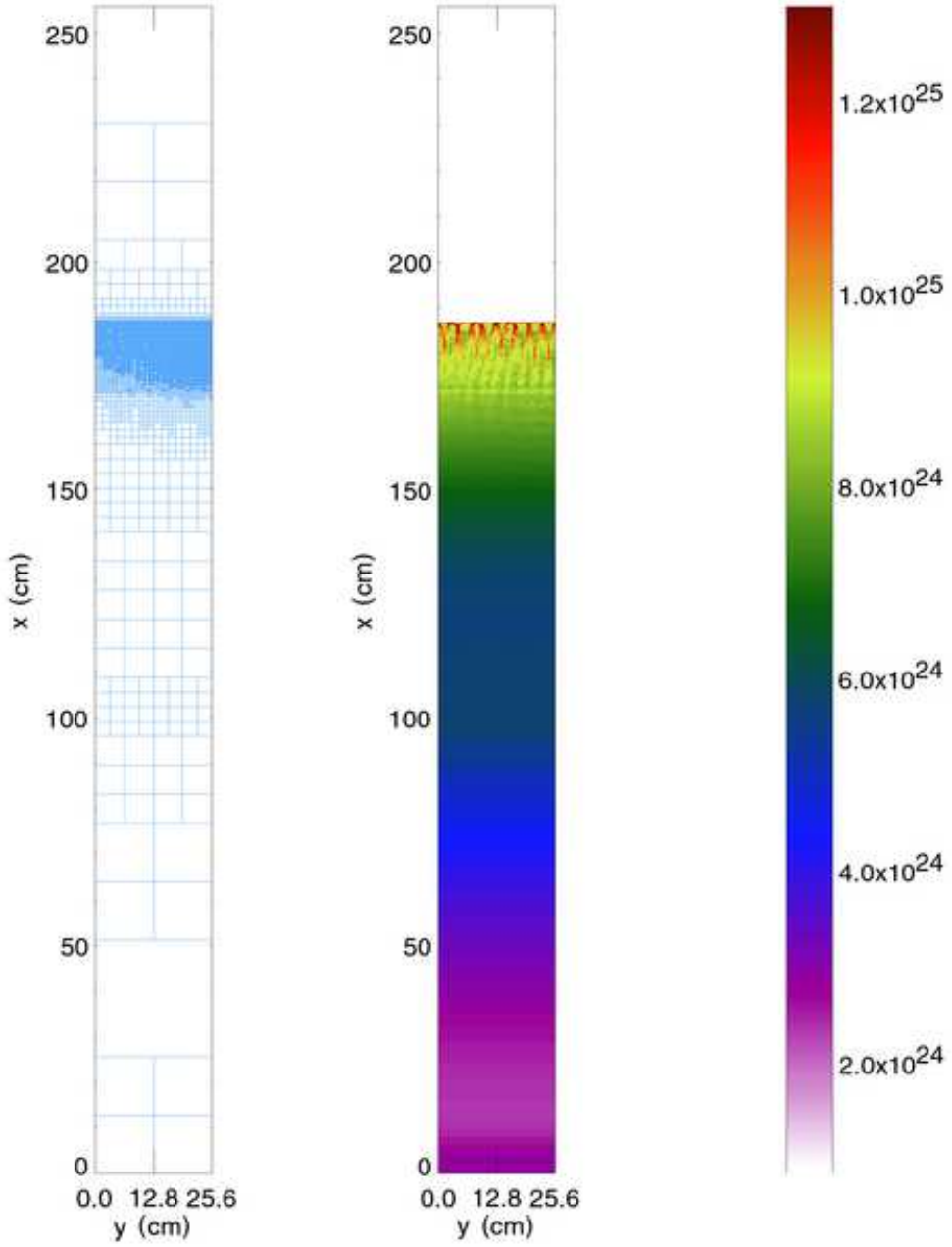

Fig. 3.— Pressure field of a detonation after 1.26×10^{-7} s. Density perturbations cause the initial conditions in Figure 2 to evolve into a complex, time-dependent structure. The interacting transverse waves extend about 25 cm behind the shock front. Full equilibration, so that the flow essentially matches the one-dimensional profiles of the ZND solution, occurs about 50 cm behind the shock front. The finest grids are placed only where there are significant changes in the thermodynamic variables. Thus, the mesh is not refined ahead of the detonation front where it is not needed, maximally refined throughout the reactive regions, and derefined behind the detonation front as the fluid flows becomes smooth.

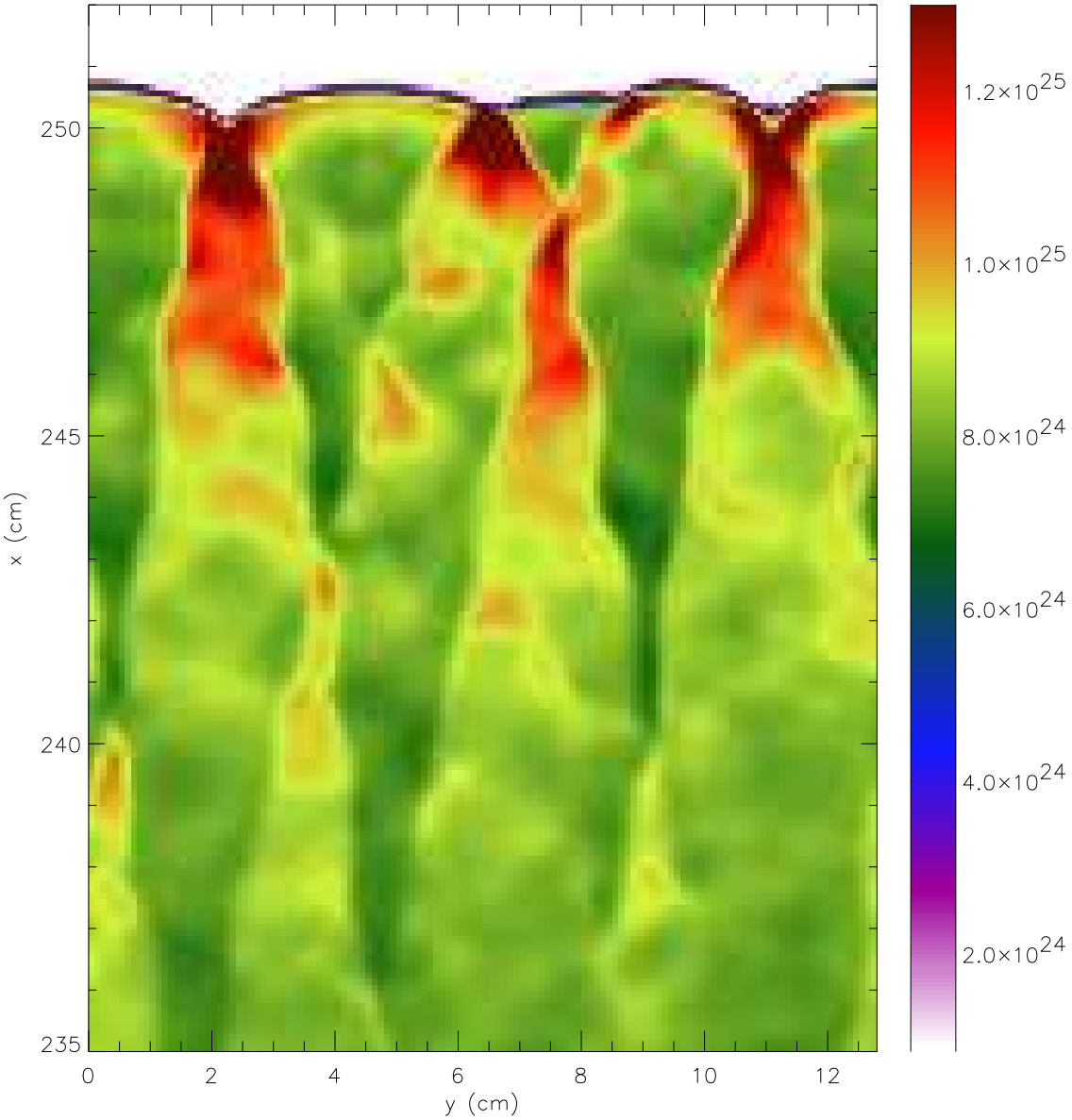

Fig. 4.— Pressure field of a detonation after 1.85×10^{-7} s with a resolution of 10^{-1} cm. The colorbar legend to the right of the plot gives the magnitude of the pressure in erg cm^{-3} on a linear scale. The weak incident shocks, transverse waves, and triple points are smeared out.

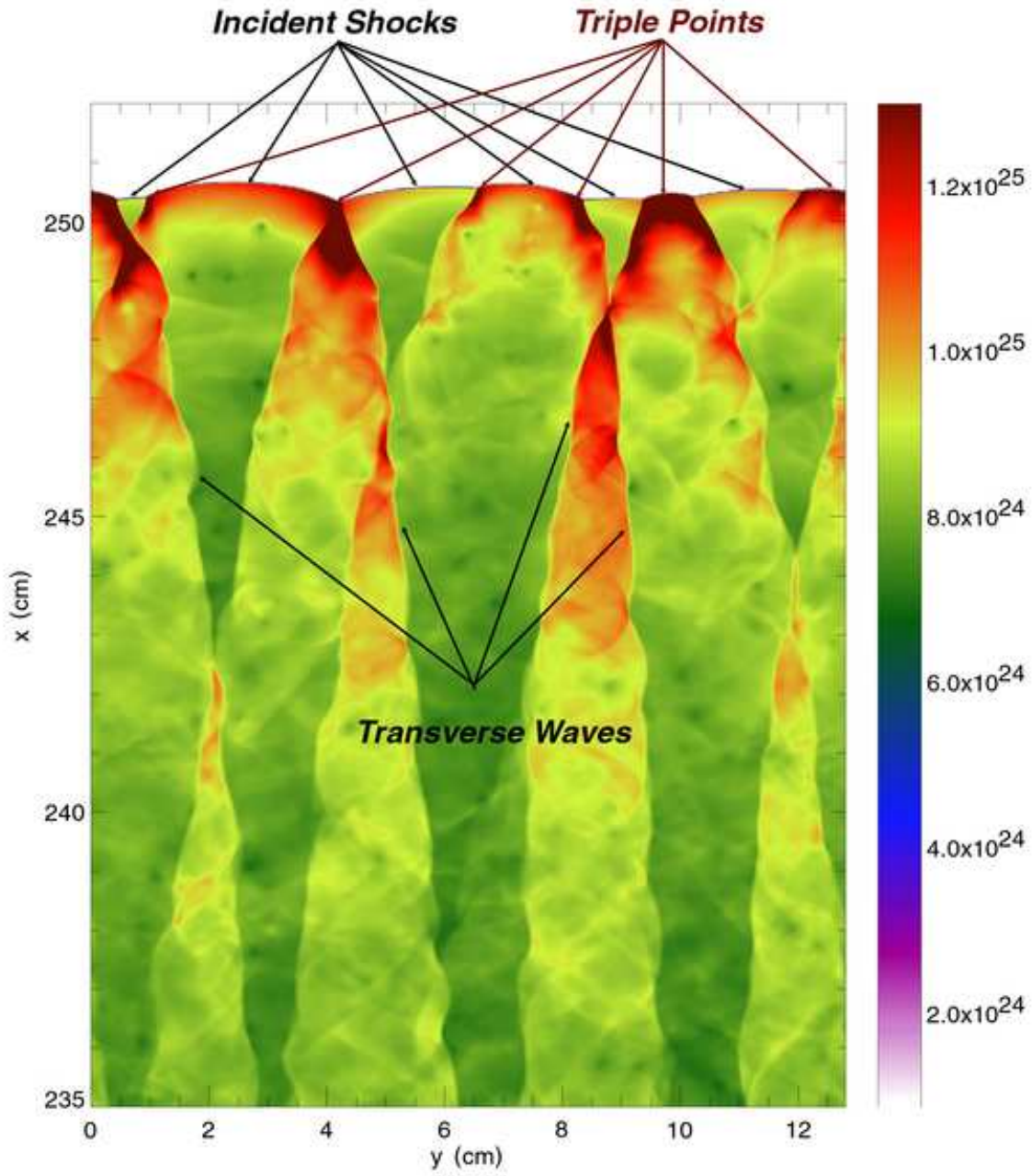

Fig. 5.— Pressure field of a detonation after 1.85×10^{-7} s with a resolution of 1.25×10^{-2} cm. The triple points appear in dark red near the head of the detonation, and are labeled by the dark red arrows. Between the triple points are the weak incident shocks, and are labelled by black arrows The transverse waves are the triangular structures that are nearly perpendicular to the detonation front, and are less noticeable in the less resolved pressure field of Figure 4. Some of the transverse waves are labelled with black arrows. Compare this figure with the schematic of Figure 1.

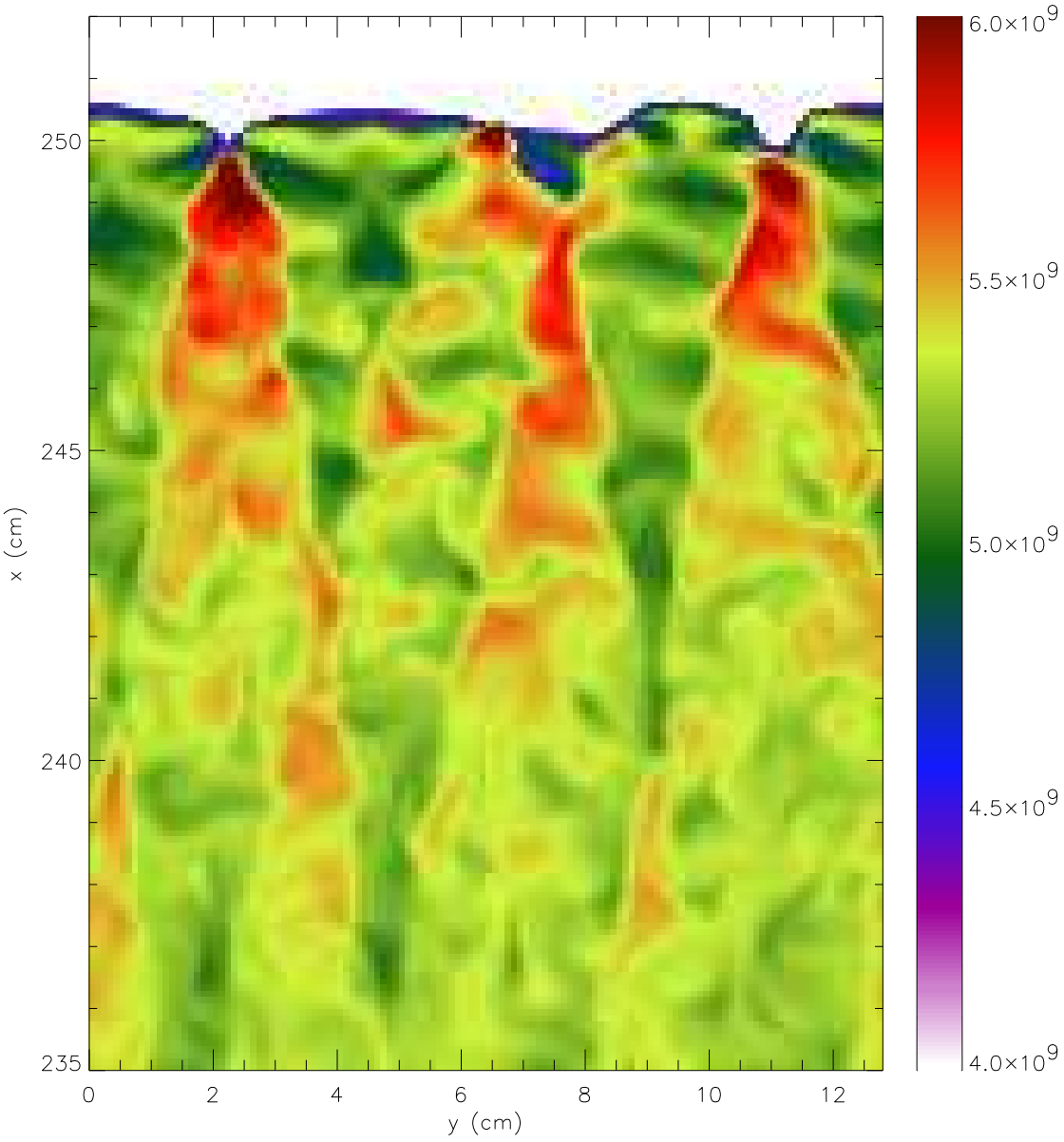

Fig. 6.— Temperature field of a detonation after 1.85×10^{-7} s with a resolution of 10^{-1} cm. The colorbar legend to the right of the plot gives the magnitude of the temperature in K on a linear scale.

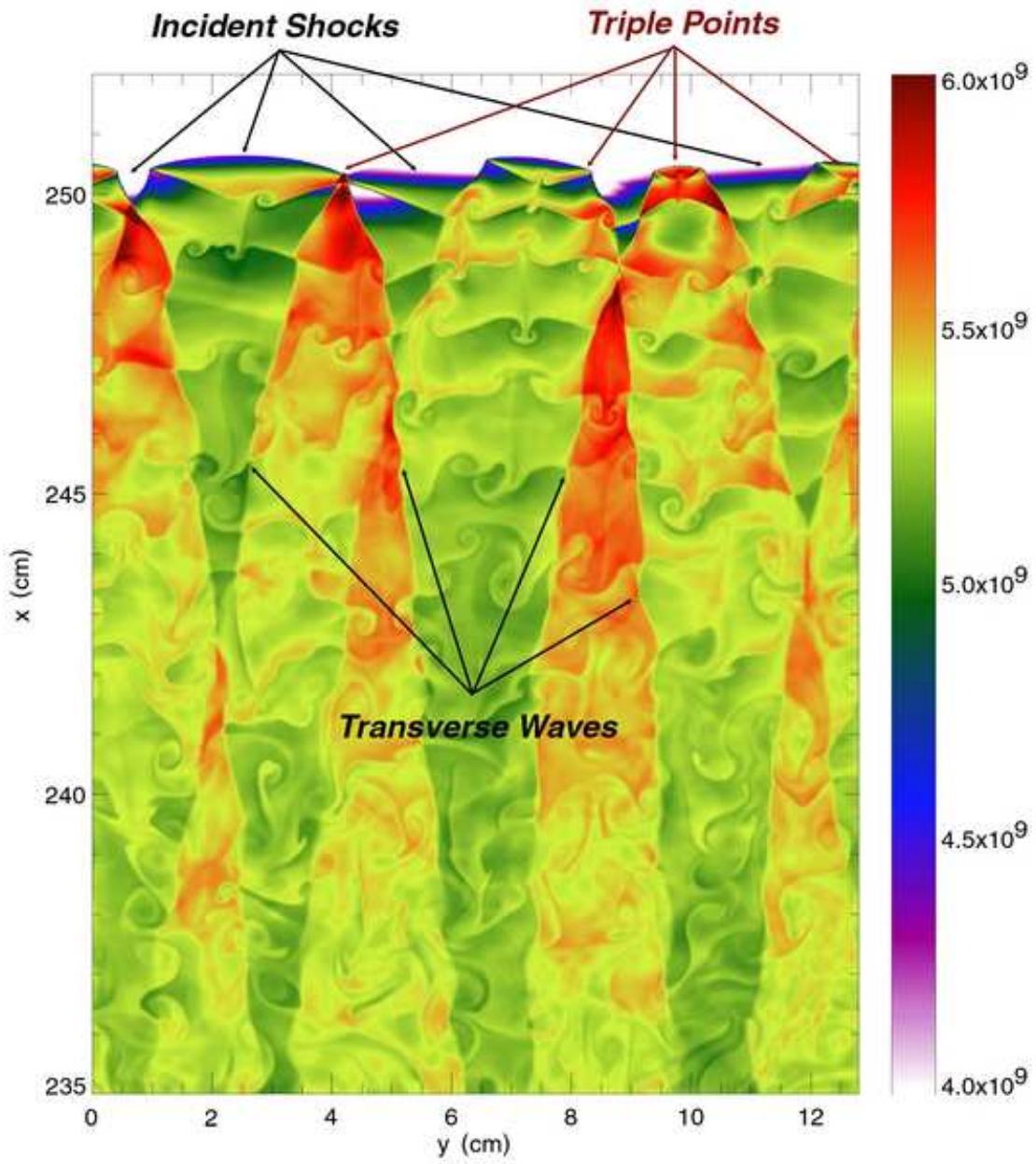

Fig. 7.— Temperature field of a detonation after 1.85×10^{-7} s with a resolution of 1.25×10^{-2} cm. Some of the triple points, weak incident shocks, and transverse waves are indicated. Compare this figure with the schematic of Figure 1. While Figure 6 shows almost no vorticity, this higher resolution case shows significant vorticity. Collisions between the transverse waves generate the vorticity, which is nearly absent in the under-resolved temperature field of Figure 6. The temperature differences generate regions with larger differences in their fuel-to-ash ratios.

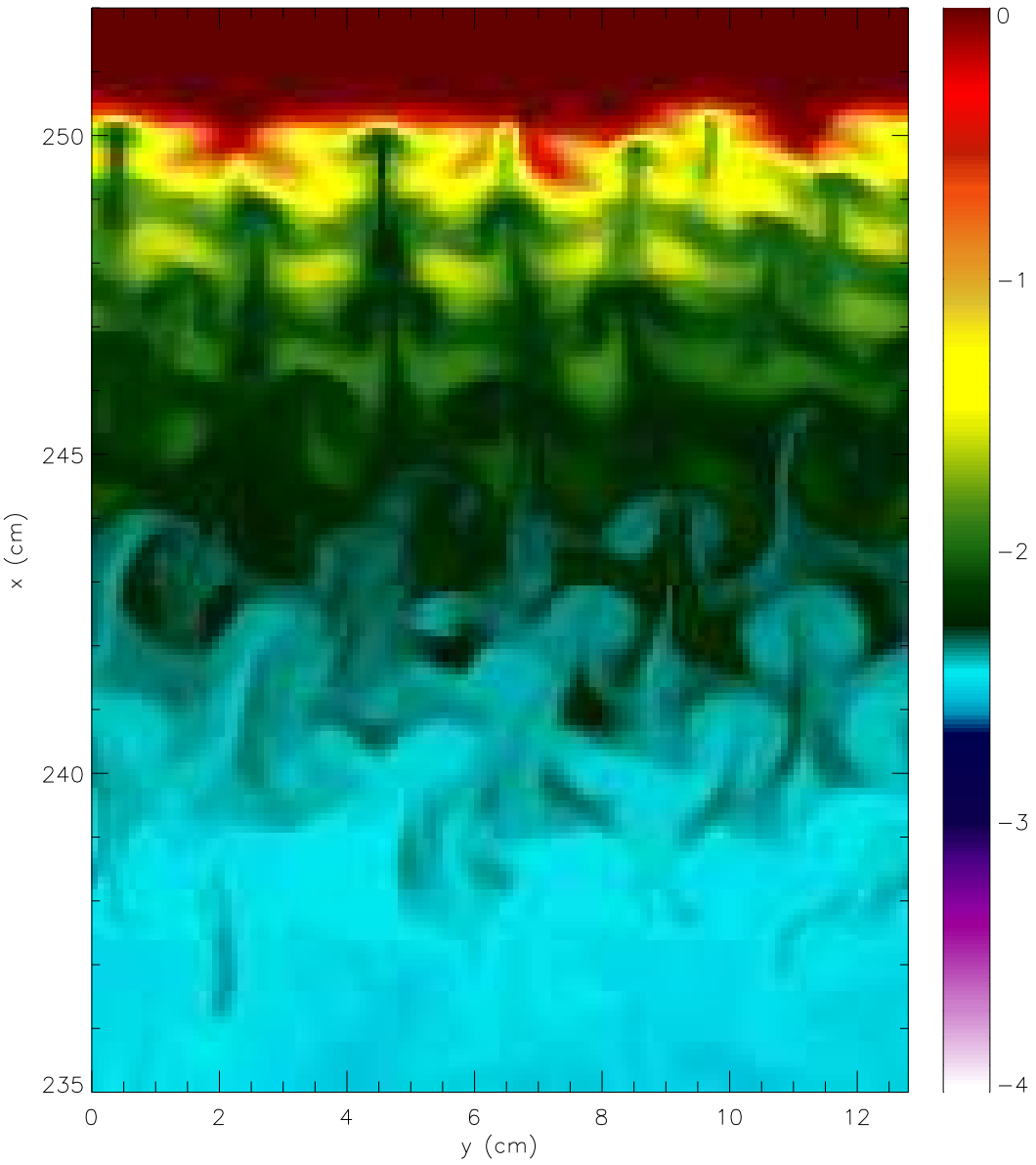

Fig. 8.— Carbon mass fraction field of a detonation after 1.85×10^{-7} s with a resolution of 10^{-1} cm. The colorbar legend to the right of the plot gives the carbon mass fraction on a logarithmic scale.

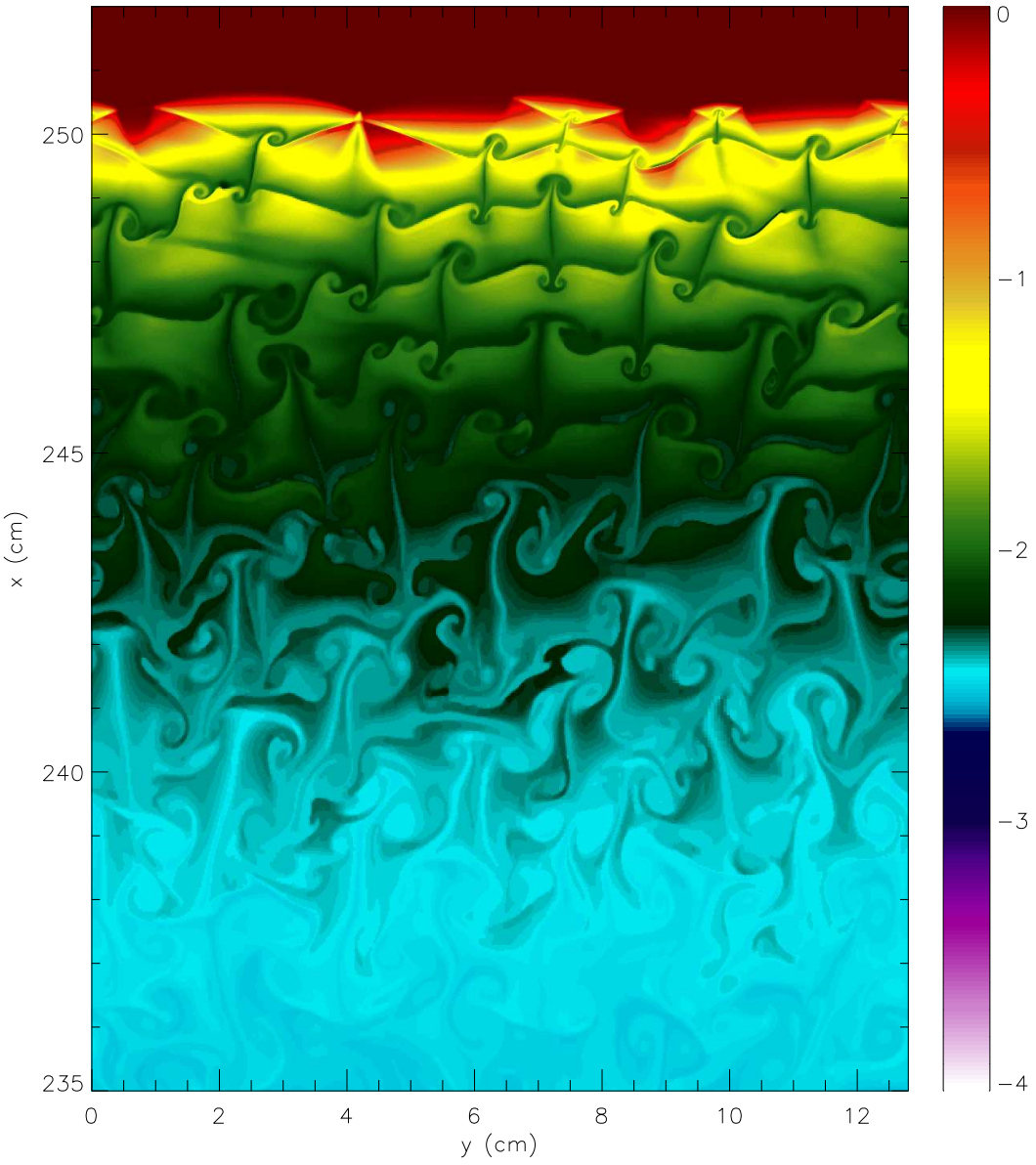

Fig. 9.— Carbon mass fraction field of a detonation after 1.85×10^{-7} s with a resolution of 1.25×10^{-4} cm.

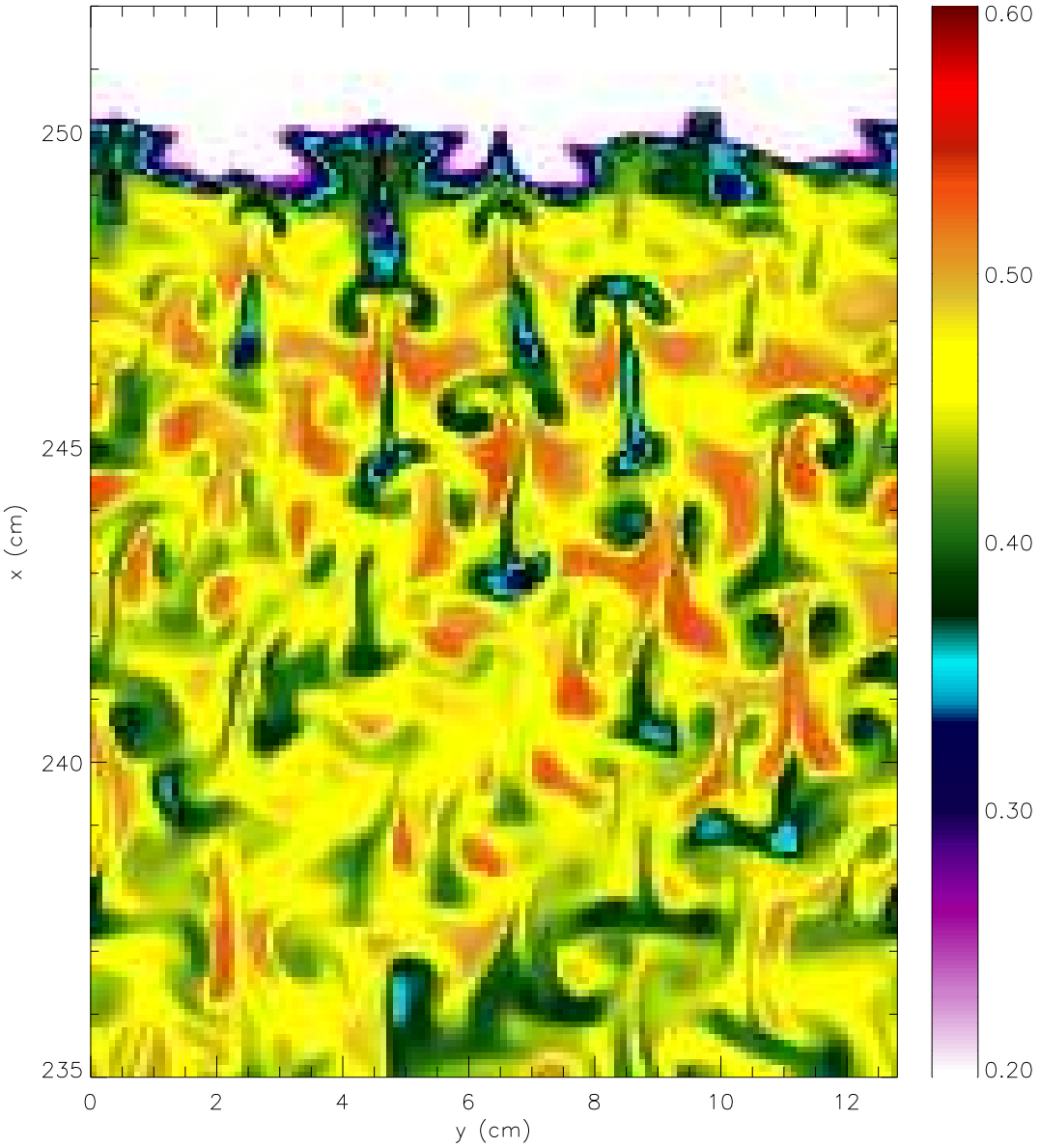

Fig. 10.— Silicon mass fraction field of a detonation after 1.85×10^{-7} s with a resolution of 10^{-1} cm. The colorbar legend to the right of the plot gives the silicon mass fraction on a linear scale.

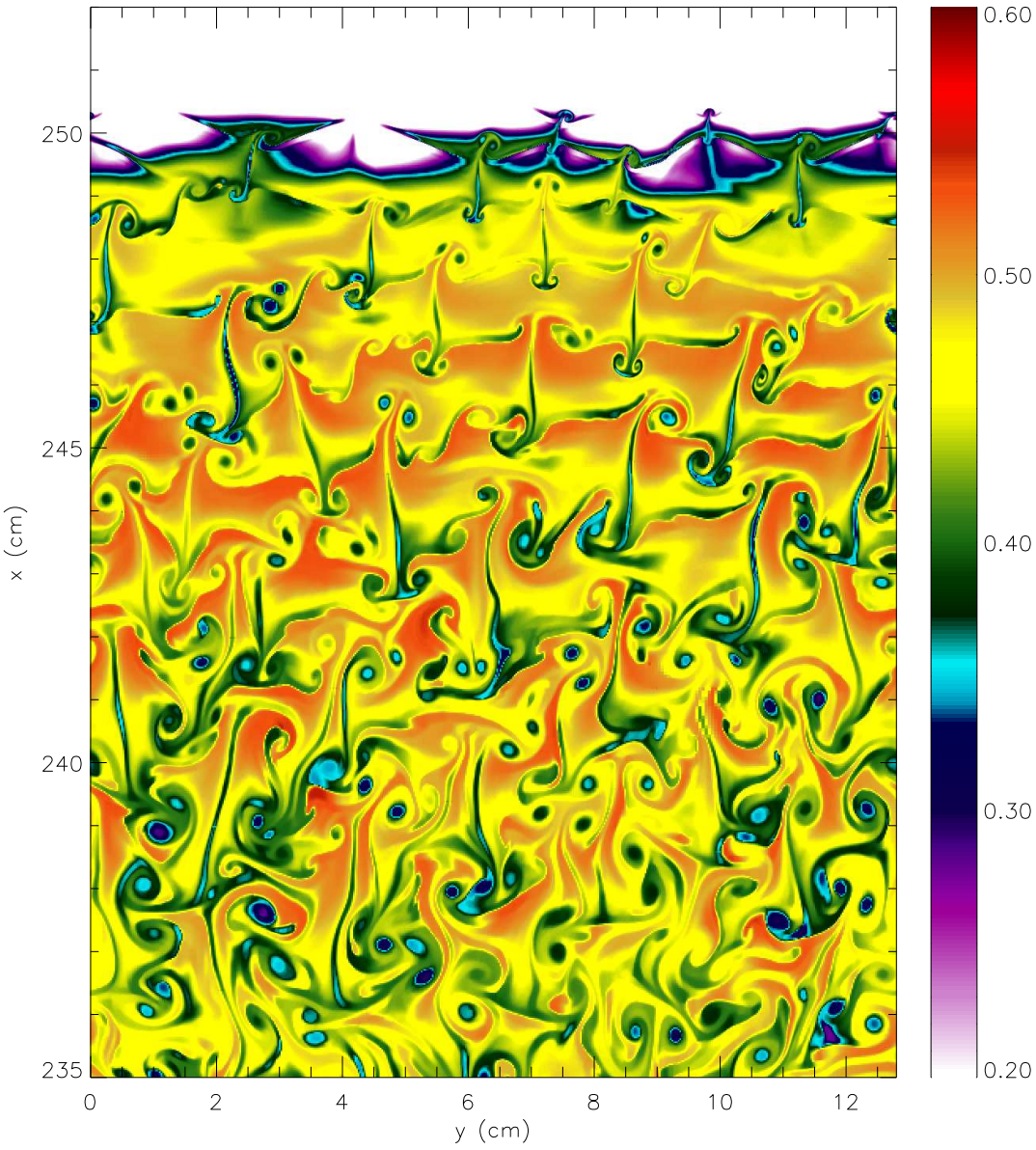

Fig. 11.— Silicon mass fraction field field of a detonation after 1.85×10^{-7} s with a resolution of 1.25×10^{-2} cm. The under-reacted regions contain more fuel than ash, while the over-reacted regions contain more ash than fuel. The swirling pattern follows the temperature vortices in Figure 7. These silicon vortices gradually disappear as the material is burned to nuclear statistical equilibrium and mixed by the velocity gradients.

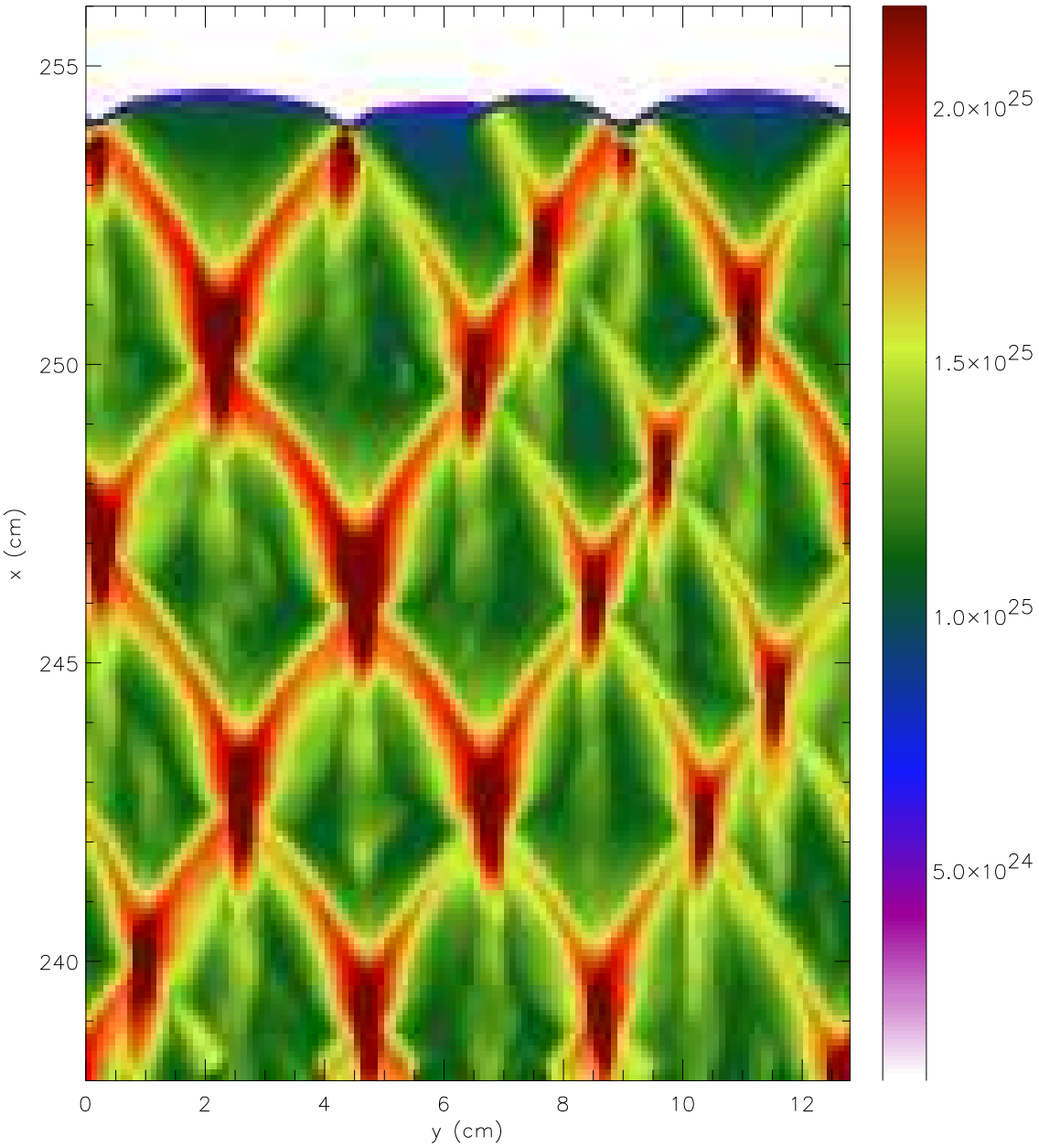

Fig. 12.— Maximum pressure reached by any point in the computational domain, for a spatial resolution of 10^{-1} cm and a temporal resolution of 5.0×10^{-11} s. The colorbar legend to the right of the plot gives the pressure on a linear scale, and the spatial resolution corresponds to 20 grid points per burning length-scale. The cellular pattern results from the trajectories of the triple points.

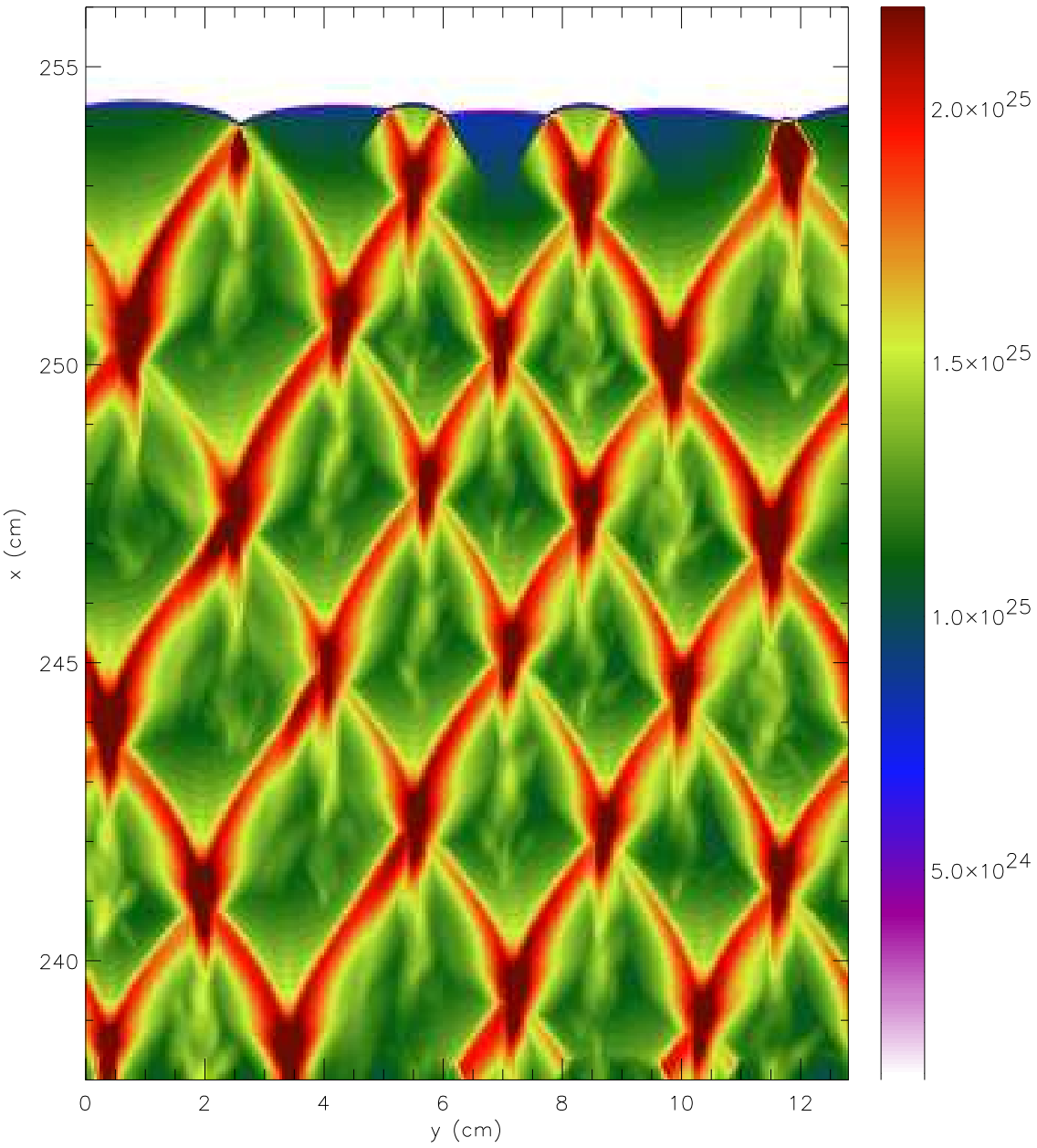

Fig. 13.— Maximum pressure reached by any point in the computational domain, for a spatial resolution of 5×10^{-2} cm and a temporal resolution of 5.0×10^{-11} s. This resolution corresponds to 40 grid points per burning length-scale. The burning length-scales set the fundamental cell sizes; the larger the burning length-scale the larger the cell sizes.

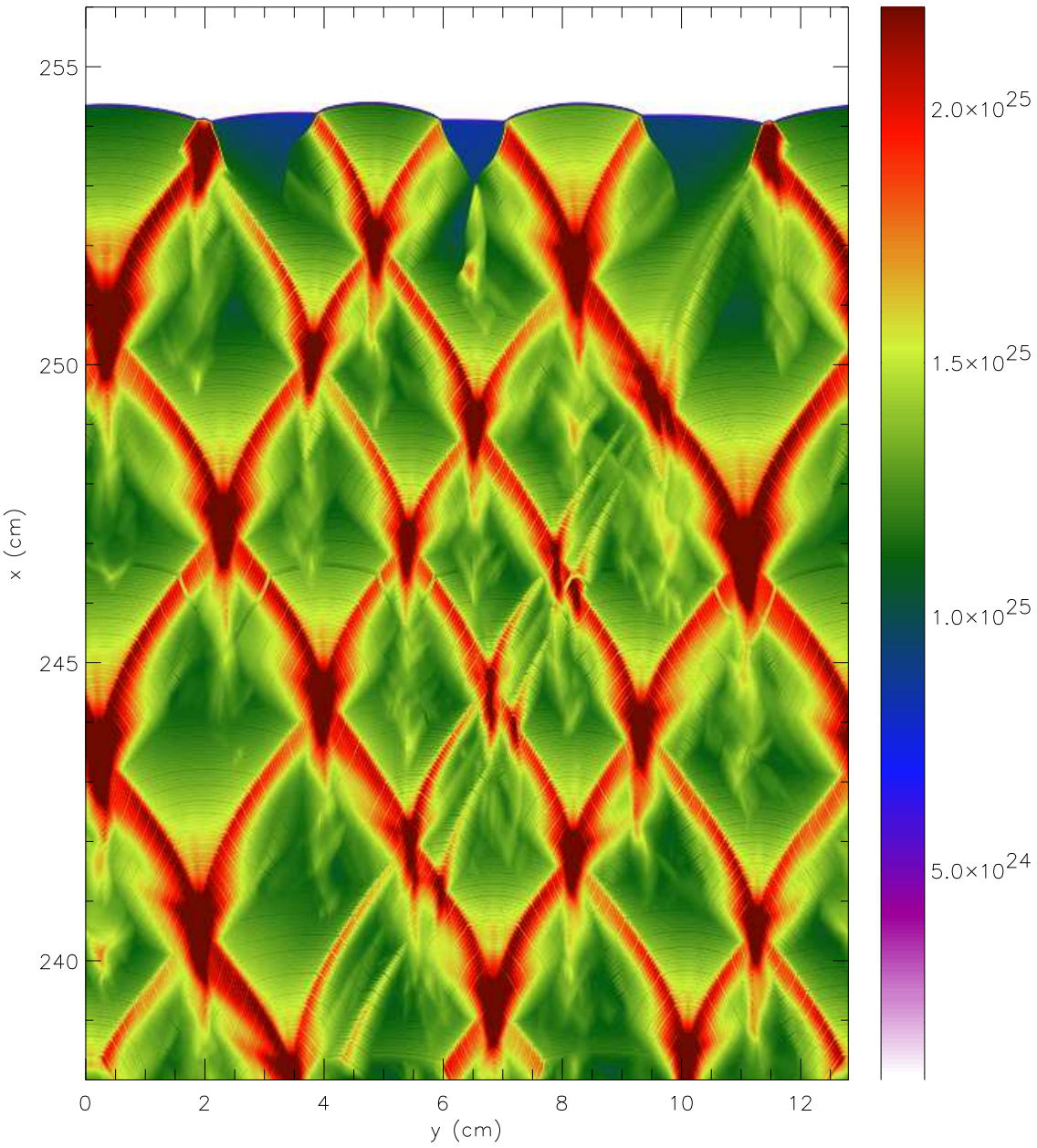

Fig. 14.— Maximum pressure reached by any point in the computational domain, for a spatial resolution of 2.5×10^{-2} cm and a temporal resolution of 5.0×10^{-11} s. The temporal resolution is visible as the striations, and the spatial resolution corresponds to 80 grid points per burning length-scale.

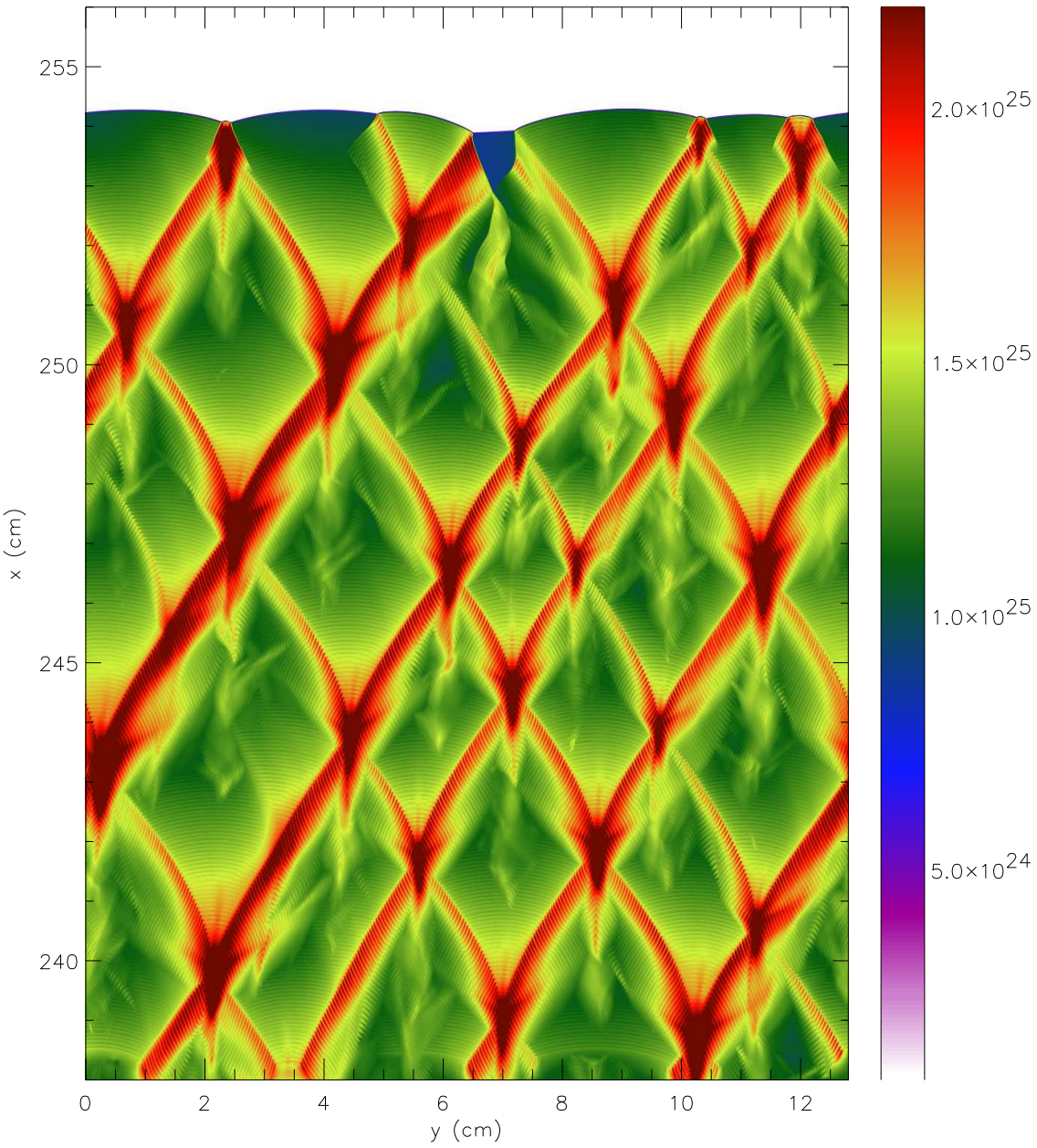

Fig. 15.— Maximum pressure reached by any point in the computational domain, for a spatial resolution of 1.25×10^{-4} cm and a temporal resolution of 5.0×10^{-11} s. The temporal resolution is visible as the striations, and the spatial resolution corresponds to 160 grid points per burning length-scale.